ENVIRONMENTAL RESEARCH
CLIMATE

PURPOSE-LED PUBLISHING™ Part of the ENVIRONMENTAL RESEARCH SERIES

PAPER • OPEN ACCESS

Global and regional thermosteric and dynamic sea level change under stratospheric aerosol injection

To cite this article: Frédéric Bonou *et al* 2025 *Environ. Res.: Climate* **4** 045013

ENVIRONMENTAL RESEARCH
CLIMATE

OPEN ACCESS

RECEIVED
20 June 2025

REVISED
12 October 2025

ACCEPTED FOR PUBLICATION
21 October 2025

PUBLISHED
31 October 2025

PAPER

Global and regional thermosteric and dynamic sea level change under stratospheric aerosol injection

Frédéric Bonou[1,2,3,*], Aubains Hounsou-Gbo[4], A Nathanael Dossa[1,2], Maiella Toupe[1,2], Marcel Kouakou[5], Arnaud Kouekam[6], Toussaint Mitchodigni[1,2], Zacharie Sohou[1,2], Alan Robock[7], Ben Kravitz[8,9], Daniele Visioni[10] and Mari Tye[11,12]

[1] Laboratory of Marine and Coastal Hydrology, Institute of Fisheries and Oceanographic Research of Benin, Cotonou 03 BP 1665, Benin
[2] International Chair in Mathematical Physics and Applications (ICMPA—UNESCO CHAIR), University of Abomey-Calavi, Abomey-Calavi 072 BP 50, Benin
[3] Laboratory of Physics and Applications (LPA), Natitingou, National University of Sciences, Technology, Engineering and Mathematics of Abomey (UNSTIM), Abomey, Benin
[4] Marine Science Institute (Labomar), Federal University of Ceará (UFC), Fortaleza, Brazil
[5] West African Science Service Centre on Climate Change and Adapted Land Use (WASCAL), Graduate Research Program on Climate Change and Disaster Risk Management, Department of Geography, Université de Lomé, Lomé 01BP1515, Togo
[6] Specialized Research Station for Fisheries and Oceanography (Marine Ecology Unit) PMB 77, Limbe, Cameroon
[7] Department of Environmental Sciences, Rutgers University, New Brunswick, NJ, United States of America
[8] Department of Earth and Atmospheric Sciences, Indiana University, Bloomington, IN, United States of America
[9] Atmospheric, Climate, and Earth Sciences Division, Pacific Northwest National Laboratory, Richland, WA, United States of America
[10] Department of Earth and Atmospheric Sciences, Cornell University, Ithaca, NY, United States of America
[11] CGD Laboratory, NSF National Center for Atmospheric Research, Boulder, CO, United States of America
[12] Whiting School of Engineering, Johns Hopkins University, Baltimore, MD, United States of America
[*] Author to whom any correspondence should be addressed.

E-mail: fredericbonou@yahoo.fr

Keywords: solar radiation modification, stratospheric aerosol injection, shared socioeconomic pathway, sea level rise, ocean heat content, regional and global variations

Supplementary material for this article is available online

Abstract

Sea level rise (SLR) is a global concern in the era of climate change, prompting the exploration of interventions such as solar radiation modification through stratospheric aerosol injection (SAI). This intervention could affect the physical system in various ways. The present study analyzes the global and regional impacts of SAI using ARISE-SAI-1.5 (SAI-1.5) simulations with the Community Earth System Model 2. We calculated the regional thermosteric sea level under different scenarios. After validating our methodology for sea level components over the period 1995–2014, we determined changes in sea level variables under both SAI-1.5 and the underlying Shared Socioeconomic Pathway 2–4.5 (SSP2-4.5) relative to the reference period (1995–2014). In contrast to sea surface temperature, which under this SAI strategy should be maintained near 1.5 °C above preindustrial values, global SLR would continue increasing under SAI-1.5. However, SAI would significantly impact thermal expansion in SSP2-4.5 simulations, reducing the global long-term sea level trend from 3.7 ± 0.03 mm yr^{-1} for SSP2-4.5–1.9 ± 0.04 mm yr^{-1} for SAI-1.5, a 49% reduction. The associated ocean heat content is reduced from $(2.0 \pm 0.3) \times 10^{22}$ J yr^{-1} under SSP2-4.5 to $(1.17 \pm 0.30) \times 10^{22}$ J yr^{-1} under SAI, a 42% reduction. Additionally, SAI would impact the regional and global ocean by reducing the SLR rate. These findings underscore the potential of SAI as a climate intervention strategy with significant implications for sea level change.

1. Introduction

Climate change driven by anthropogenic greenhouse gas emissions induces sea level rise (SLR) at the global scale [1]. Rising temperatures are causing the expansion of ocean water and the melting of land-based glaciers and ice sheets, leading to global mean SLR (GMSLR) that could reach over 1 m by the

end of this century under high emissions scenarios [2]. The current rate of GMSLR is primarily driven by three main factors: ocean thermal expansion (accounting for about 50% of the rise), melting of glaciers and ice sheets (contributing approximately 44%), and changes in land-water storage responsible for around 8% [1, 3]. The sea level changes will have profound impacts on coastal communities and ecosystems around the world [4].

In response to the mounting climate crisis, there has been growing interest in exploring climate intervention strategies, such as solar radiation modification (SRM) through stratospheric aerosol injection (SAI) [5]. By injecting reflective aerosols into the upper atmosphere, SAI has the potential to offset the global temperature increases and therefore associated SLR [6]. Some previous studies have investigated the effects of solar geoengineering on SLR under different scenarios, particularly focusing on SAI and solar dimming [3], showing that SRM could significantly reduce the rate of global thermosteric SLR by 36%–41% by the end of the century compared to a high greenhouse gas scenario (SSP5-8.5). In their work, Visioni *et al* showed that the G6sulfur scenario (a scenario under which temperatures are reduced from those under the SSP5-8.5 scenario to those under the SSP2-4.5 scenario by means of SAI) [7]) showed a stronger reduction in the rate of SLR, especially in the Arctic Ocean and mid-latitude regions, while G6solar (which uses solar dimming instead) exhibited reductions primarily eastward from mid-latitude South America. Their research highlighted that while geoengineering might mitigate SLR, it could not completely eliminate regional variations or reverse SLR that has already occurred, with some coastal areas still facing significant risks. Overall, their findings underscored the potential of SRM as a tool for climate change mitigation, though challenges remain in its implementation and governance [3]. The regional and global sea level response to SAI is still not well understood, as changes in ocean circulation will also affect regional sea level [8]. Irvine *et al* [9] highlighted a critical trade-off in SAI deployment in trying to reduce SLR: while surface cooling may reduce the rate of SLR, the associated changes in radiative forcing and surface fluxes can alter ocean energetics in ways that exacerbate subsurface warming or shift regional sea level patterns. These unintended consequences underscore the need for diagnostics that go beyond surface metrics to capture depth-resolved heat redistribution and regional variability.

There is a lack of comprehensive studies on the spatial and temporal patterns of sea level response to SAI, especially concerning specific regional variations. Understanding these patterns is crucial for evaluating the effectiveness of SAI in different regions and for assessing its potential impacts on coastal communities, ecosystem, economies and habitats and livelihoods [2, 10]. The main contributors driving the responses in sea level changes due to SAI are yet to be explored in depth. This includes, for instance, the effects of SAI on ocean circulation, ice sheet dynamics, and other physical processes that influence sea level, both at the local and global levels. Therefore, SAI impacts on sea level under different scenarios of SAI implementation need to be better investigated.

The objective of this study is to determine how SAI impacts global and regional thermosteric and dynamic sea level (DSL) using the Community Earth System Model version 2 (CESM2) [11] by determining the changes under Shared Socioeconomic Pathway 2–4.5 (SSP2-4.5) [12] and the SAI scenario Assessing Responses and Impacts of Solar climate intervention on the Earth system with SAI 1.5 (ARISE-SAI-1.5, referred to in this article as SAI-1.5) experiments, described in Richter *et al* [13]. In contrast to Yue *et al* [3], where regional SLR was estimated from the summation of global mean thermosteric and spatial dynamical sea level, in this study we calculate directly thermosteric sea level (TSL) regionally from salinity, temperature and density. The next sections will present the methods and data we employed in this work (section 2), the model output evaluation and its results under the analyzed scenarios (section 3), a critical discussion of the results and summary (section 4).

2. Methods and data

2.1. Model description

CESM2 with the Whole Atmosphere Community Climate Model version 6 (WACCM6) [14] is a state-of-the-art global climate model developed by the National Center for Atmospheric Research and other collaborating institutions [11, 14]. It incorporates multiple Earth system components, including the atmosphere, ocean, land, sea ice, and biogeochemistry, to provide a comprehensive representation of the Earth's climate system. The CESM2 (WACCM6) [15] model uses prognostic aerosols represented by the Modal Aerosol Model version 4. It also includes a comprehensive chemistry module with interactive tropospheric, stratospheric, mesospheric, and lower-thermospheric chemistry, featuring 228 prognostic chemical species. The ocean component of the model is based on the Parallel Ocean Program version 2, as described in Danabasoglu *et al* [11]. This coupled Earth system model provides a detailed representation of the atmospheric composition, dynamics, and interactions with the ocean, enabling investigations

on various aspects of the climate system. It combines a detailed atmospheric model including the upper atmosphere (WACCM6) with a sophisticated ocean model to simulate the coupled physical, chemical, and dynamical processes of the atmosphere and ocean. CESM2 currently only accounts for ice melting processes in Greenland but has yet to integrate those for Antarctica. At present, the freshwater generated from the melting ice in Greenland is introduced into the ocean; however, there are limitations in how this interacts with the ocean model [11]. Since the model does not fully account for ice melt processes, we do not analyze the SLR component related to mass inputs from melting glaciers and ice sheets.

2.2. Historical simulation

The present study used the monthly output of the historical simulations covering the period from 1850 to 2014 from CESM2 (WACCM6) [14]. These simulations used observed historical forcings, including changes in greenhouse gases, aerosols, solar variability, land use, and volcanic eruptions. The historical CESM2 simulations have been extensively evaluated and compared to observational data [11, 14]. Studies have shown that the model is able to reasonably capture the observed trends and variability in surface temperature, precipitation, sea ice extent, and other key climate variables over the historical period [11, 14]. The tropospheric physics are the same as in the low-top version, the Community Atmosphere Model version 6, which is usually used in such evaluations [14]. Three members of the historical simulation have been used for temperature, salinity, sea level pressure, and DSL (sea surface height) data, essential for estimating sea level components and validating climate models.

2.3. SSP2-4.5 simulation

The SSP2-4.5 scenario serves as a control simulation that reflects a moderate emissions trajectory [12]. The SSP2-4.5 scenario is characterized by a balanced approach to socioeconomic development, with emissions that are projected to stabilize at a level that results in a global mean temperature increase of 2.65 K above pre-industrial temperatures by 2069 [12]. The CESM2 model is also employed in this scenario, providing a baseline against which the impacts of SAI can be compared, the reference against which the changes of simulations can be determined. These simulations were run from 2015 to 2070 using a 10-member ensemble [13].

2.4. SAI-1.5 simulation

The ARISE-SAI-1.5 scenario is designed to evaluate the effects of SAI on climate. The SAI simulations is branched from the SSP2-4.5 scenario beginning in 2035 and ending in 2070 [13]. Its goal is to prevent global-mean surface temperatures increasing more than 1.5 K above pre-industrial levels [16]. This simulation operates under the premise of injecting sulfur dioxide gas into the stratosphere at approximately 21.5 km altitude [13, 16], which then converts to sulfate aerosols. The aerosol injection takes place at four specific latitudes: 15°N, 30°N, 15°S, and 30°S. The simulation employs a feedback-control mechanism that adjusts the amount of aerosol deployment to achieve three primary climate objectives: stabilizing global temperatures, preserving the north-south temperature gradient between hemispheres, and maintaining the temperature gradient from the equator to the poles. The ARISE-SAI-1.5 simulations consist of an ensemble of 10 members [11].

2.5. Observational data

This work utilizes monthly Sea Surface Height data from the Global Ocean Ensemble Physics Reanalysis at 0.25° × 0.25° resolution for the years 1995–2014. The ensemble comprises four reanalyzes with monthly means of Temperature, Salinity, Currents and Ice variables for 75 vertical levels [17].

The EN4 dataset is a comprehensive collection of global ocean subsurface temperature and salinity measurements spanning from 1900 to the present day [18–21]. It compiles data from multiple sources including Argo floats, XBTs, CTDs, and marine stations and applies bias corrections and quality control measures to generate gridded monthly fields at a spatial resolution of 1° × 1°. Compiled at a monthly resolution, the dataset combines data from various observational sources, including autonomous floats, oceanographic surveys, and historical archives. A key component of the EN4 dataset is the database of quality-controlled *in-situ* ocean profiles. These profiles undergo rigorous quality assurance checks to ensure the reliability of the measurements, with flags indicating the level of data confidence. The dataset also includes spatially complete analyses of temperature and salinity, gridded at a 1° resolution with 42 depth levels covering the region from the Southern Ocean to the Arctic. This work used data from 1995–2014 to validate the simulated ocean temperatures and salinity.

Table 1. List of CESM2 simulations and observations data with their different periods.

Experiments	Members	Validation period	Baseline	Future
Historical	3	1995–2014	—	—
SAI-1.5	10	—	—	2050–2069
SSP2-4.5	10	—	2020–2039	2050–2069
Copernicus data	—	1995–2014	—	—
EN4 data	—	1995–2014	—	—

2.6. Methods

In this study, we used a DSL variable, sea surface height above the geoid (also called zos) over the period from 1995 to 2014 for historical experiments (3 members, table 1), from 2015 to 2069 for SSP2-4.5 (10 members, table 1), and from 2035 to 2069 for SAI-1.5 (10 members, table 1). The geoid is an idealized model of Earth's shape that represents mean sea level and serves as a reference for measuring sea surface height and geostrophic flows. CESM2 incorporates the POP2 ocean model, which takes the geoid into account when calculating sea surface height and ocean currents. The model's ability to simulate the interactions between the atmosphere, oceans, and land is enhanced by using a geoid reference that reflects Earth's shape and gravitational field [11]. Thermosteric, steric, halosteric and inverse barometer sea level components have been calculated from temperature, salinity, and sea surface pressure according to the methodology described below and in Griffies & Greatbatch [22]. This assumes mass conservation of the global ocean and, therefore, does not account for the effects of melting glaciers and ice sheets. Thermosteric and steric sea level have been corrected using the inverse barometer according to Yue *et al* [3].

We calculate steric, thermosteric, halosteric sea level, and inverse barometer based on methods used in Griffies and Greatbatch [21] and Griffies and Greatbatch [22] using CESM 2 models for historical, SSP2-4.5 and SAI-1.5 simulations. All the sea level components changes have been calculated related to the reference period of 1995–2014.

2.7. Local steric sea level changes calculation

The local steric sea level is calculated according to equation (1):

$$\eta^{steric}(\tau) = \eta\left(\tau^{ref}\right) - \frac{1}{\rho_0}\sum dz\left[\rho(\theta,S,p) - \rho\left(\theta^{ref},S^{ref},p^{ref}\right)\right] \tag{1}$$

where:

$\eta^{\text{steric}}(\tau)$ is the sea level change at time τ,
$\eta\left(\tau^{\text{ref}}\right)$ is sea level height at the reference state,
(θ,S,p), are potential temperature, salinity, and pressure
$\left(\theta^{\text{ref}},S^{\text{ref}},p^{\text{ref}}\right)$, are potential temperature, salinity, and pressure at the reference state
ρ_0 is the global constant reference density (1035 kg m^{-3})

This relationship is used in momlevel, an open-source Python tool designed to compute sea level-related fields using data from MOM6.

The local TSL is given by equation (2):

$$\eta^{\text{thermosteric}}(\tau) = \eta\left(\tau^{\text{ref}}\right) - \frac{1}{\rho_0}\sum \text{d}z\left[\rho\left(\theta,S^{\text{ref}},p^{\text{ref}}\right) - \rho\left(\theta^{\text{ref}},S^{\text{ref}},p^{\text{ref}}\right)\right]. \tag{2}$$

The local halosteric sea level is given by equation (3):

$$\eta^{\text{halosteric}}(\tau) = \eta\left(\tau^{\text{ref}}\right) - \frac{1}{\rho_0}\sum \text{d}z\left[\rho\left(\theta^{\text{ref}},S,p^{\text{ref}}\right) - \rho\left(\theta^{\text{ref}},S^{\text{ref}},p^{\text{ref}}\right)\right] \tag{3}$$

$\eta^{\text{thermosteric}}$ is the impact on sea level due to temperature changes. $\eta^{\text{halosteric}}$ is the same for salinity changes.

We adjusted the temperature to account for model drift, which can occur due to the gradual adjustment of the deep ocean or an inadequate representation of energy conservation in the model simulation [3, 23, 24]. Therefore, we have corrected all scenarios, using the standard "linear drift correction based on pre-industrial simulation data over 500 years.

In CESM2, physical variables such as potential temperature (theta), salinity, and pressure (depth) are computed per grid cell and per vertical ocean level, rather than per basin or fixed depth. The ocean model uses a structured 3D grid with nominal 1° horizontal resolution and 60 vertical layers. These layers are defined by model-specific depth levels that vary with bathymetry and are consistent across the global domain. Pressure is derived at each level based on hydrostatic equilibrium and local density. Basin depth influences the number of active layers in each column, but all variables are resolved on the model-defined vertical coordinate system, ensuring consistency in diagnostics across regions and ensemble members.

2.8. Global steric sea level

Global steric sea level change is based on methods of calculation used in Yue *et al* [3], which is calculated in equation (4):

$$\eta^{B}_{diag}(\tau) \approx \eta^{B}(\tau) + \frac{V^{0}}{A} ln\left(\frac{\langle\rho\rangle^{0}}{(\rho(\tau)}\right) \tag{4}$$

where:

$\eta^{B}_{\mathrm{diag}}(\tau)$ is the diagnosed sea level at time τ
V^{0} is the initial reference volume of the global ocean
A is the global surface area of the ocean
$\langle\rho\rangle^{0}$ is the initial global mean density
$\langle(\rho(\tau)\rangle$ is the global mean density at time τ.

2.9. Inverse barometer effect

The inverse barometer effect on sea level is the ocean's response to atmospheric pressure variations at the surface [22, 25]. Regional variations in atmospheric mass will cause regional variations in ocean sea level due to the inverse barometer effect. Similarly, changes in sea ice coverage lead to pressure perturbations at the ocean surface. The inverse barometer effect is represented by equation (5):

$$\eta^{IB} = \frac{-p_{atm}}{\rho(S,T,P) * g} \tag{5}$$

where p_{atm} is the full atmospheric pressure and ρ is the density at the ocean surface. In practice, it is common to consider *in situ* ocean density (ρ_0) at the top model layer as this quantity is commonly saved from ocean models.

2.10. Ocean heat content (OHC)

OHC refers to the amount of heat energy stored in the world's oceans [19, 26]. It is a crucial metric for understanding Earth's energy balance and climate change. OHC is computed using the following equation (6)

$$OHC = C\int_{Z_1}^{Z_2} \rho(z).T(z)\,dz \tag{6}$$

where OHC is ocean heat content in Joule m^{-2},

ρ is the density is obtained
C is the specific heat of sea water, 3990 J $(\mathrm{kg\ K})^{-1}$,
z_1 is the depth of the top of the layer in meters,
z_2 is the depth of the bottom of the layer in meters,
and T is the temperature at each depth in degrees Kelvin.

The Mann–Kendall test has been used to estimate the trends of sea level and OHC under different scenarios. This test is a non-parametric statistical method used to identify monotonic trends in time series data without assuming a specific data distribution [27] and is particularly useful for analyzing environmental data that do not conform to a Normal (Gaussian) distribution, such as sea level and

OHC Additionally, we calculated the percentage reduction in calculated trends under SAI compared to SSP2-4.5 as shown in equation (7):

$$Percentage\ Reduction = \frac{Trend_{SSP2-4.5} - Trend_{SAI-1.5}}{Trend_{SSP2-4.5}} \times 100 \tag{7}$$

where:

$Trend_{SSP2-4.5}$ is the trend value for the SSP2-4.5 scenario.
$Trend_{SAI-1.5}$ is the trend value for the SAI-1.5 scenario.

In this study, we also analyze the surface net energy fluxes (Q_{NET}), which accounts for the combination of net longwave flux (Q_L), net solar flux (Q_S), net surface sensible heat flux (Q_H), surface latent heat flux (Q_E). The equation for Q_{NET} can be expressed as follows:

$$Q_{NET} = Q_L + Q_S + Q_H + Q_E. \tag{8}$$

We have analyzed Q_{NET} to evaluate how energy inputs and outputs vary under different climate scenarios, specifically SSP2-4.5 and SAI-1.5.

The ocean heat budget (W m^{-2}) is calculated as follows [28] :

$$\frac{\partial\,(\mathrm{OHC})}{\partial t} = \boldsymbol{Q}_{NET} - \boldsymbol{Q}_v + \boldsymbol{Q}_{winstress} + \in . \tag{9}$$

Here, $\frac{\partial(OHC)}{\partial t}$ denotes the rate at which the ocean gains (positive value) or loses (negative value) heat, where OHC is the ocean heat content from surface to 5500 m, Q_{NET} represents the net heat fluxes at the ocean surface, Q_v is the divergence of heat transport, and $\in$ represents the residual term, which includes unresolved processes, model errors, and inaccuracies in the calculation. For the global ocean, Q_v is zero because it only redistributes heat within the ocean and does not contribute to a net gain or loss of heat. $Q_{winstress}$ is the wind energy transfer from the atmosphere to the ocean.

Wind energy transfer from the atmosphere to the ocean $\boldsymbol{Q}_{winstress}$ was computed as the scalar product of surface wind stress and ocean surface velocity vectors [29]:

$$\boldsymbol{Q}_{winstress} = \tau_x u + \tau_y v \tag{10}$$

where τ_x and τ_y are the zonal and meridional components of wind stress (N m^{-2}), and u and v are the corresponding ocean surface velocities (m s^{-1}). For each model grid cell, the resulting energy transfer field $\boldsymbol{Q}_{winstress}$ was expressed in watts per square meter (W m^{-2}). All variables were extracted at the ocean surface layer and temporally subset to match the respective scenario periods. The diagnostics focus on monthly wind stress (TAUX, TAUY) and ocean surface velocity (UVEL, VVEL). For the historical simulation period (1995–2014), three ensemble members (r1–r3) were used. For SSP2-4.5 (2015–2069) and SAI-1.5 (2035–2069), all ten members were processed per scenario.

3. Results

3.1. Dynamic and TSL validation

Figure 1 provides a spatial distribution of DSL and the trend of combined DSL and TSL from 1995 to 2014. The comparison of the historical simulations and observations suggests a good agreement between the model and observations in capturing the spatial distribution of DSL during the 1995–2014 period (figures 1(a) and (b)). These two top maps indicate strong positive DSL in the western tropical Atlantic and eastern North Atlantic with the DSL values varying between 20 and 100 cm. Conversely, regions such as the Southern Ocean and parts of the equatorial Pacific exhibit negative DSL anomalies, with values ranging from −20 to −100 cm (figures 1(a) and (b)).

Figures 1(c) and (d) show that CESM2 does not properly capture the large-scale pattern of DSL + TSL trends relative to observations in some regions, while observational variability higher and model skill lower especially in the Southern Hemisphere. Conversely, the model captures well positive DSL + TSL trends in the western tropical Pacific, the western North Atlantic, and parts of the Southern Ocean, alongside weaker or negative trends elsewhere. In the Pacific, apparent out-of-phase behavior between modeled and observed trends can arise from wind-driven DSL variability and internal variability as well as the offline reconstruction of steric height, which does not include dynamic adjustment. Accordingly, regional DSL + TSL anomalies should be interpreted cautiously.

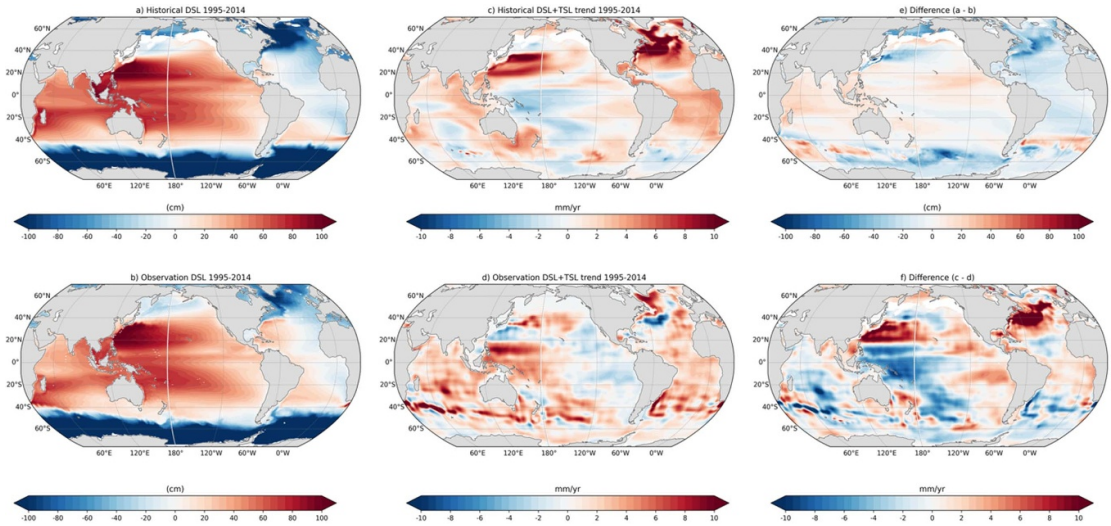

Figure 1. Spatial distribution of dynamic sea level (DSL) from 1995 to 2014 for: (a) the historical simulation and (b) Copernicus Marine Environment Monitoring Service (CMEMS) observations. The middle panels are the trend (1995–2014) distribution of the sum of DSL and thermosteric sea level (TSL) for (c) the historical simulation, and for (d) observations of DSL + TSL (DSL from CMEMS and TSL from EN4). (e) Difference between a and b (a), (b). (f) Difference between c and d (c), (d).

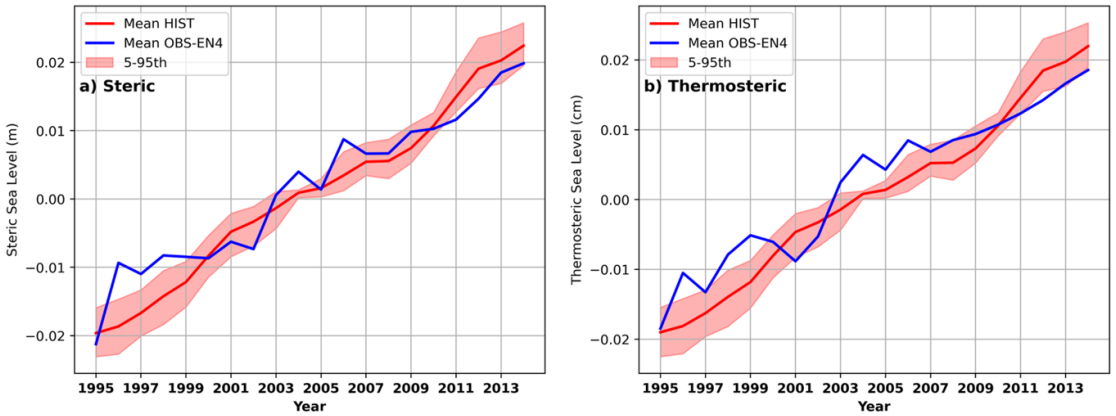

Figure 2. Global (a) steric and (b) thermosteric sea level from historical simulations (red) with that of EN4 observations (blue). The shaded pink area represents the 5–95th percentile range of the CESM2 ensemble, indicating the uncertainty bounds around the mean HIST trend.

Figure 2 presents a comparison of the global mean sea level trends between historical simulations and observations for two different sea level components: steric and thermosteric. In the steric sea level component (panel a) the red line, which represents the mean historical trend in CESM2, shows a gradual increase in sea level over the years from 1995 to 2014 with the trend value of 2.18 ± 0.03 mm yr^{-1}. The blue line, which represents the mean observed steric sea level, also exhibits a similar increasing pattern, though slightly lower in magnitude (2.01 mm yr^{-1}). In the TSL component (panel b), the model's sea level trend 2.13 ± 0.03 mm yr^{-1} is similar to that of observations 2.03 mm yr^{-1}. Interannual variability for the individual simulations is effectively removed by using the ensemble mean of 10 ensemble members. The historical simulation shows reasonable agreement with observations, although, as discussed above, some regions show notable difference particularly in the thermosteric component, highlighting areas where model performance could be improved.

3.2. Global thermosteric and OHC under SSP2-4.5 and SAI-1.5

Figure 3 presents the projected global mean TSL and OHC changes under two different climate scenarios, SSP2-4.5 (2015–2069) and SAI-1.5 (2035–2069). SSP2-4.5 projects a steady increase in TSL and OHC calculated for the 0–5500 m layer during the 55 year period. The SAI-1.5 simulations also project increases in the thermosteric component (figure 3(a)), but at a considerably slower rate of increase compared to the SSP2-4.5 scenario (1.9 ± 0.04 mm yr^{-1} for SAI-1.5 against 3.7 ± 0.03 mm yr^{-1} for

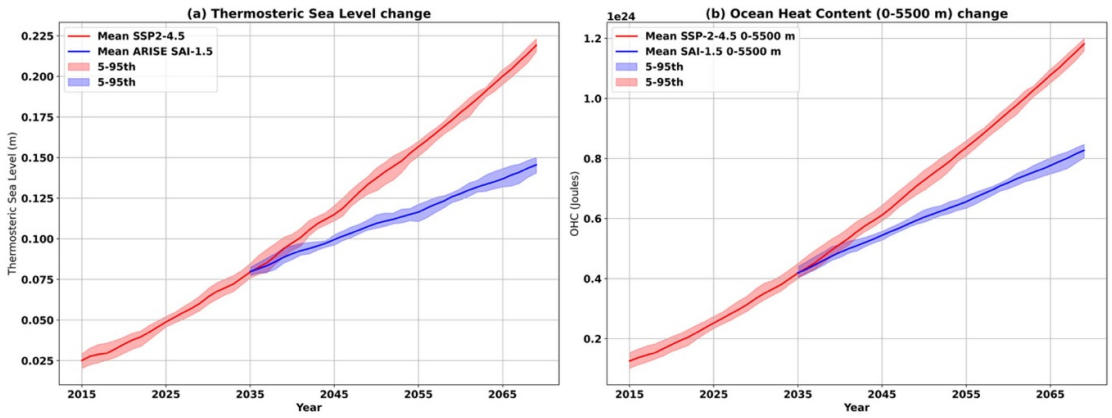

Figure 3. Time series of global (a) thermosteric sea level (m) and (b) ocean heat content (in 10^{24} Joules), relative to 1995–2014. The shaded area represents 5th and 95th percentile ensemble range.

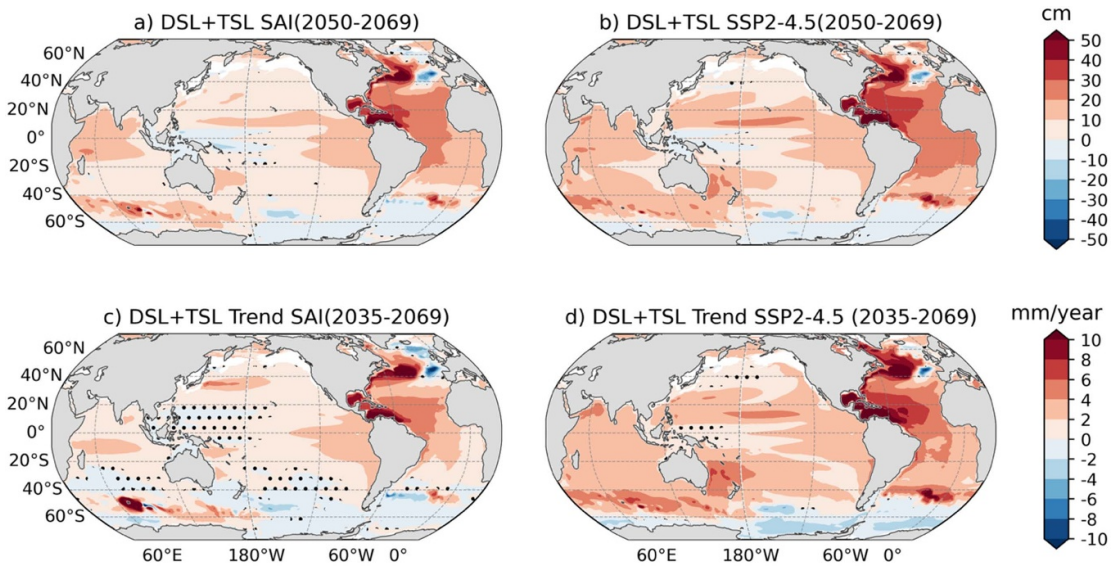

Figure 4. For SAI and SSP2-4.5, (a) and (b) Spatial distribution of dynamic and thermosteric sea level (DSL + TSL) rise for the period 2050–2069 and (c) and (d) trend of DSL + TSL over 2035–2069. Stipple points indicate regions where changes in sea level trends are not statistically siginificant within different members at the 95% confidence level, determined using a t-test.

SSP2-4.5). This is effectively a 51% of reduction in the rate of SLR under SAI-1.5. Similarly, the rate of increase in OHC for 0–5500 m is also dampened in the SAI-1.5 scenario compared to the SSP2-4.5 scenario, with rates of $(1.17 \pm 0.30) \times 10^{22}$ J yr^{-1} and $(2.00 \pm 0.03) \times 10^{22}$ J yr^{-1} respectively for SAI-1.5 and SSP2-4.5, a 42% reduction.

3.3. Spatial distribution of dynamic and TSL under SAI-1.5 and SSP2-4.5

Figure 4 shows maps of the projected changes in SLR under different climate scenarios from 2050 to 2069. Figures 4(a) and (b) show similar spatial patterns, with regions in the Pacific, Atlantic, and Indian Oceans exhibiting higher SLR, particularly in the tropics and subtropics, reaching up to 50 cm increase in the tropical and northwestern Atlantic Ocean under both scenarios. Figures 4(c) and (d) present the projected local linear trends in SLR from 2035 to 2069 for SAI and SSP2-4.5 scenarios. Both scenarios project rapid rates of SLR along the Atlantic coast of North America, but slower rates of SLR under SAI-1.5 than SSP2-4.5 in other parts of the ocean. The trends range from approximately -10 mm yr^{-1} to $+10$ mm yr^{-1}, with the fastest rates of rise persisting in the Atlantic Ocean regions. These maps highlight the spatial variability in the rate of SLR, with some regions experiencing higher rates of change than others. The SSP2-4.5 scenario again shows a high trend, with larger areas exhibiting higher rates of SLR compared to the SAI scenario.

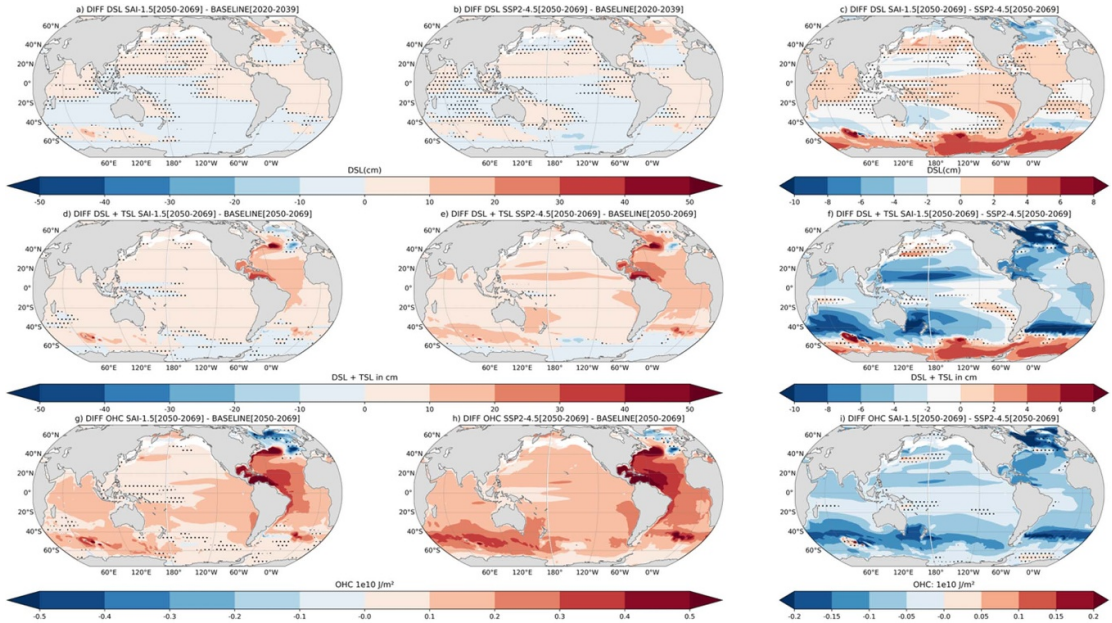

Figure 5. Spatial distribution of dynamic sea level (DSL) (a) difference between SAI-1.5 (2050–2069) and BASELINE (2020–2039), (b) difference between SSP2-4.5 (2050–2069) and BASELINE (2020–2039) and (c) difference between SAI-1.5 (2050–2069) and SSP2.4.5 (2050–2069). Spatial distribution of DSL + TSL (d) difference between SAI-1.5 (2050–2069) and BASELINE (2020–2039), (e) difference between SSP2-4.5 (2050–2069) and BASELINE (2020–2039) and (f) difference between SAI-1.5 (2050–2069) and SSP2.4.5 (2050–2069). Spatial distribution of ocean heat content (10^{10} J m^{-2}): (g) difference between SAI-1.5 (2050–2069) and BASELINE (2020–2039), (h) difference between SSP2-4.5 (2050–2069) and BASELINE (2020–2039) and (i) difference between SAI-1.5 (2050–2069) and SSP2.4.5 (2050–2069) of ocean heat content (J m^{-2}). Stipple points indicate regions where changes in sea level variables are not statistically siginificant within different members at the 95% confidence level, determined using a t-test.

3.4. Impact of SAI on dynamic and TSL: spatial distribution

Figures 5(a)–(c) present the spatial projected changes in DSL, providing crucial insights into potential future impacts of climate change. In figure 5(a) increased DSL is apparent mostly in the Atlantic Ocean. Figure (b) presents a similar analysis. Figure 5(c) shows significant positive changes in DSL with SAI across many regions, particularly in low-lying coastal areas such as the eastern United States, where sea-level rise is already a pressing concern. The spatial analysis indicates that these regions will likely face heightened risks of flooding and erosion, exacerbated by ongoing climate change.

Figures 5(d)–(f) compare the projected total sea level changes under the SAI-1.5 and SSP2-4.5 scenarios, as well as across different time periods. The combined DSL + TSL is lower in the SAI-1.5 scenario primarily in the Pacific, Atlantic, and Indian Oceans (figure 5(f)). It should be noted that DSL changes are relatively minor compared to TSL. This suggests that SAI intervention could reduce the projected increases in sea level in these major ocean basins. Figure 5(e) presents the difference in DSL + TSL between the 2050–2069 SSP2-4.5 scenario and the 2020–2039 baseline. The positive change in the southern region (60° S–90° S) in (figure 5(c)) is essentially due to the change in DSL. These results demonstrate that while SAI may moderate the rate of projected increases in sea level across most ocean basins, there are spatial differences with some low-lying regions potentially experiencing similar rapid SLR under an SAI scenario.

Figures 5(g)–(i) show differences in OHC. Under the SAI-1.5 scenario, the North Atlantic shows a moderate increase in OHC compared to the baseline period (figure 5(g)). This suggests that SAI-1.5 has a stabilizing effect on OHC in this region. In contrast, the SSP2-4.5 scenario results in a greater increase in heat content (figure 5(h)). This scenario indicates a higher accumulation of heat in the deep ocean, potentially affecting ocean circulation patterns and marine ecosystems. The equatorial Pacific shows a slight increase in heat content under the SAI-1.5 scenario, indicating that this scenario could help to reduce some of the warming effects in this region. The Southern Ocean exhibits a relatively stable heat content under the SAI-1.5 scenario, with only minor increases compared to the baseline. In contrast, the SSP2-4.5 scenario shows a significant increase in heat content in the Southern Ocean, which would melt sea ice.

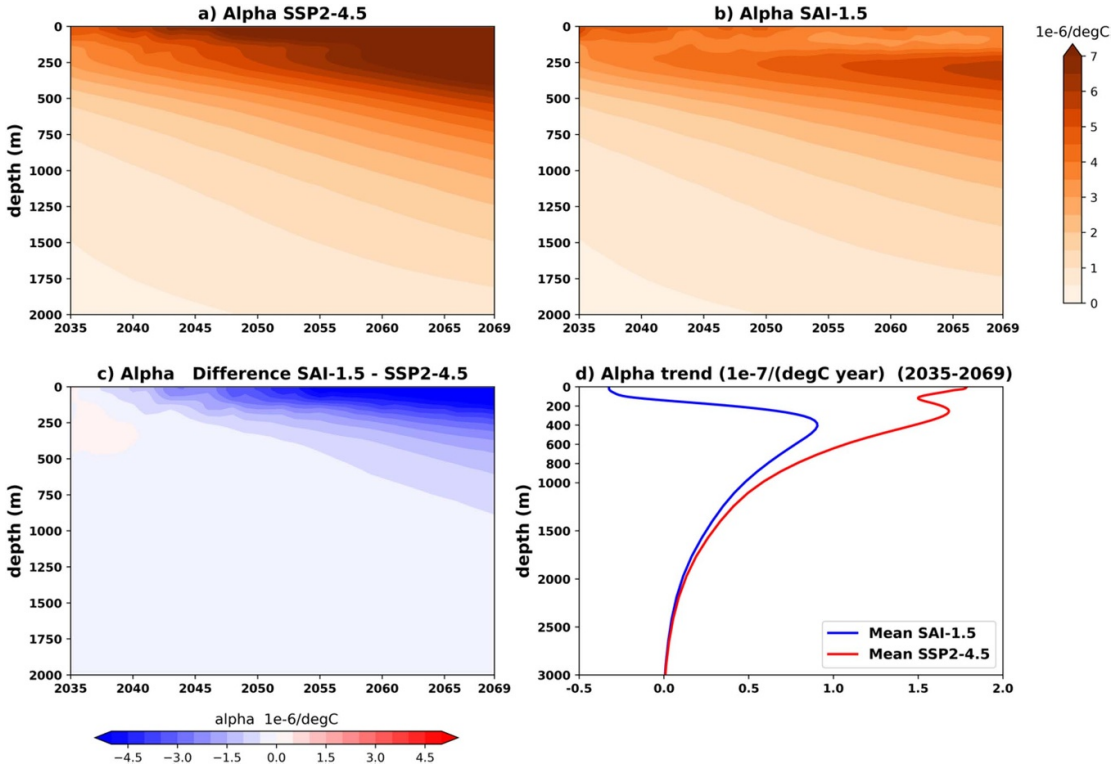

Figure 6. Vertical distribution of the thermal expansion coefficient change (α, 10^{-6} °C^{-1}) for (a) SAI-1.5 and (b) SSP2-4.5 and (c) the difference over the period of 2035–2069; and (d) global vertical thermal expansion of SAI-1.5 (blue) and SP2-4.5 (red) for the period 2035–2069. The *x*-axis represents the rate of thermal expansion coefficient per year (10^{-7} °C yr^{-1}).

3.5. Impact of SAI on sea level: vertical distribution

Figures 6(a)–(c) present the vertical distribution of the thermal expansion coefficient for the period 2035–2069, for SAI-1.5 and SSP2-4.5. Figures 6(a) and (b) show a big difference between the SAI-1.5 and SSP2-4.5 scenarios from the ocean surface down to around 2000 m, with SAI showing weaker rates of increase in the coefficient of thermal expansion. Under SAI-1.5, the thermal expansion coefficient in the upper 200 m is reduced due to surface cooling, freshening, and enhanced stratification, which collectively suppress the temperature sensitivity of seawater density and limit vertical mixing of warmer subsurface layers. The large differences from the surface to 400 m highlight the impact of SAI at the ocean upper layer (figure 6(c)). From around 2000 m to the deep ocean, both profiles become similar. Figure 6(d) presents the global vertical profile of the thermal expansion coefficient average over the period 2035–2069, for SAI-1.5 and SSP2-4.5. These figures show that the contribution of thermal expansion in the upper 2000 m would still continue under SAI-1.5 at a similar rate as that of SSP2-4.5.

To explore how the thermal expansion coefficient changes with latitude and depth, figure 7 illustrates its distribution (°C^{-1}) across different latitudes and depths under SSP2-4.5 and SAI-1.5 scenarios. In SSP2-4.5, the thermal expansion coefficient increases over the first 1000 m of depth, with deeper changes observed in the extratropical regions of both hemispheres and shallower changes in the tropical zone (figure 7(a)). Under SAI-1.5, the vertical and latitudinal distribution of the thermal expansion coefficient is similar to that of SSP2-4.5, though with weaker values overall (figures 7(a) and (b)). SAI-1.5 reduces the thermal expansion coefficient compared to SSP2-4.5, with the largest differences occurring in the extratropical regions (figure 7(c)). The larges reductions in the rate of thermal expansion are in the Northern Hemisphere, while in the tropical region, the reduction is limited to a very shallow ocean layer. This suggests that SAI-1.5 will have minimal impact on SLR due to thermal expansion in the tropical area, but could be most effective in extratropical regions, potentially mitigating the rate of SLR.

Figure 8(a) shows the impact of the SAI-1.5 and SSP2-4.5 scenarios on sea surface temperature (SST) changes relative to the reference period from 1995 to 2014, showing that SAI could counteract warming and even cool SSTs in certain regions compared to the baseline. To emphasize the contribution of subsurface heat accumulation to SLR under SAI-1.5, figure 8(b) presents the change in OHC across different depth layers relative to the reference period from 1995 to 2014. The upper layer (0–200 m), which directly influences SSTs and marine life, shows no significant increase in OHC under SAI-1.5, indicating that surface heat gain is effectively offset. In contrast, the deeper layer (200–2000 m) shows a substantial

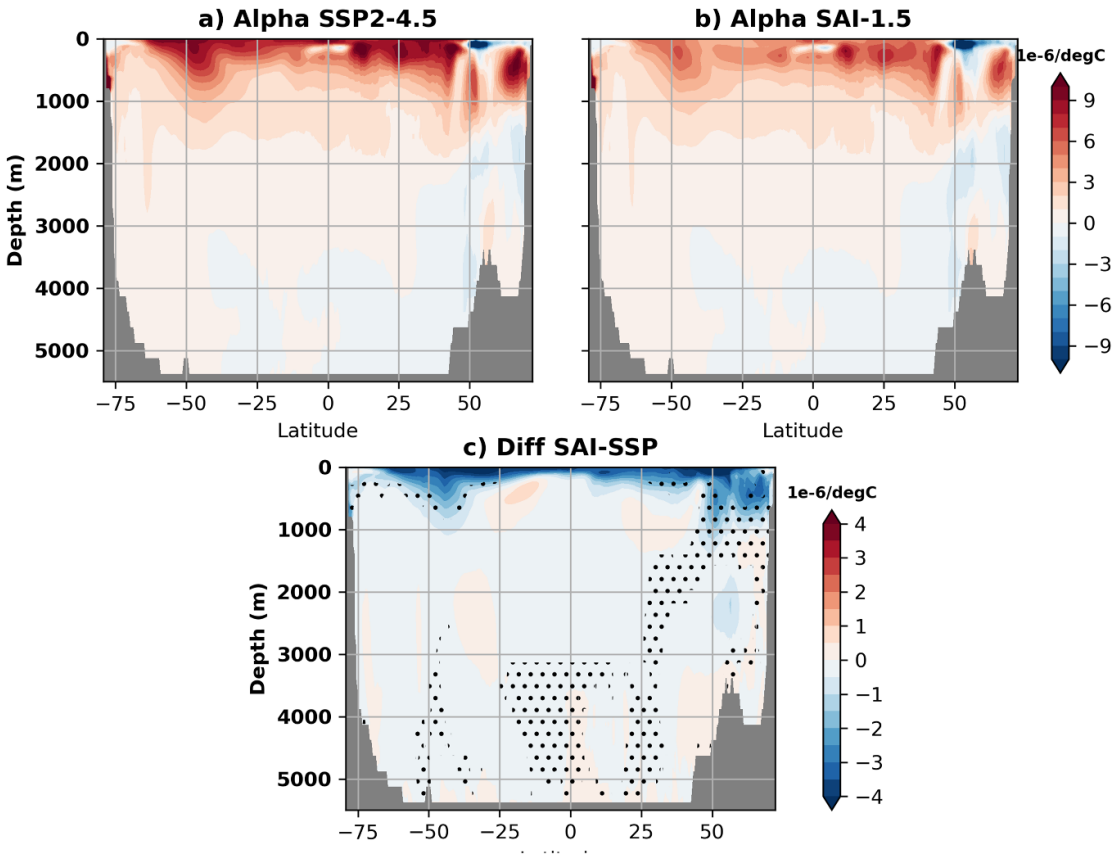

Figure 7. Latitude-depth distribution of thermal expansion coefficient (α, $°C^{-1}$), relative to 1995–2014: (a) SAI-1.5 and (b) SSP2-4.5 and the difference between SAI-1.5 and SSP2-4.5 from 2050 to 2069. Stipple points indicate regions where differences within different members are not statistically significant at the 95% confidence level, determined using a t-test.

increase in OHC under the SSP2-4.5 scenario (1.68×10^{22} J yr^{-1}), while SAI-1.5 shows a smaller positive trend (1.16×10^{22} J yr^{-1}), suggesting mitigation of deep ocean heat accumulation. Increases in sea level under SAI are primarily driven by thermosteric changes originating from OHC accumulation in the 200–2000 m layer (figures 2(a) and (b)), rather than surface warming. This pattern highlights that while SAI alters surface conditions, its influence on subsurface ocean heating and associated steric SLR is less pronounced.

Figure 8(c) presents the net energy flux (Q_{NET}) changes relative to the reference period from 1995 to 2014 for SSP2-4.5 associated to table 2. The Q_{NET} values show no trend for the SAI-1.5 scenario, indicating that solar radiation management could effectively reduce the net energy absorbed by the ocean. In contrast, the SSP2-4.5 scenario exhibits a relative increase in Q_{NET} over time, aligning with the projected rise in greenhouse gas emissions. All variables have been estimated relative to the mean reference period from 1995 to 2014.

Figures 8(a)–(d) collectively illustrate the differences between SAI-1.5 and SSP2-4.5 in terms of projected SST, OHC, and net energy flux and tendency of OHC. SAI-1.5 demonstrates a capacity to stabilize SST and limit OHC increases in the upper 200 m layers, while effectively reducing net energy absorption. In contrast, SSP2-4.5 projects a concerning trend of rising of SSTs and OHC, driven by continued greenhouse gas emissions.

The absence of a linear trend in SST and upper-OHC in the 0–200 m layer, alongside an increase in full-depth OHC under SAI-1.5, motivates an evaluation of the global ocean heat budget. This budget is estimated by assuming that the rate of heat gain or loss in the ocean is equal to the net surface heat fluxes (Q_{NET}) at the ocean-atmosphere interface, plus a residual term.

Under the SSP2-4.5 scenario, Q_{NET} and the OHC tendency exhibit the same linear trend, but with a nearly constant offset, represented by the residual (figure 8(c)). This indicates that the long-term trend in global ocean heat gain is primarily driven by net surface fluxes, while other processes contribute additional heat at a steady rate. In contrast, under the SAI-1.5 scenario, neither Q_{NET} nor the OHC tendency

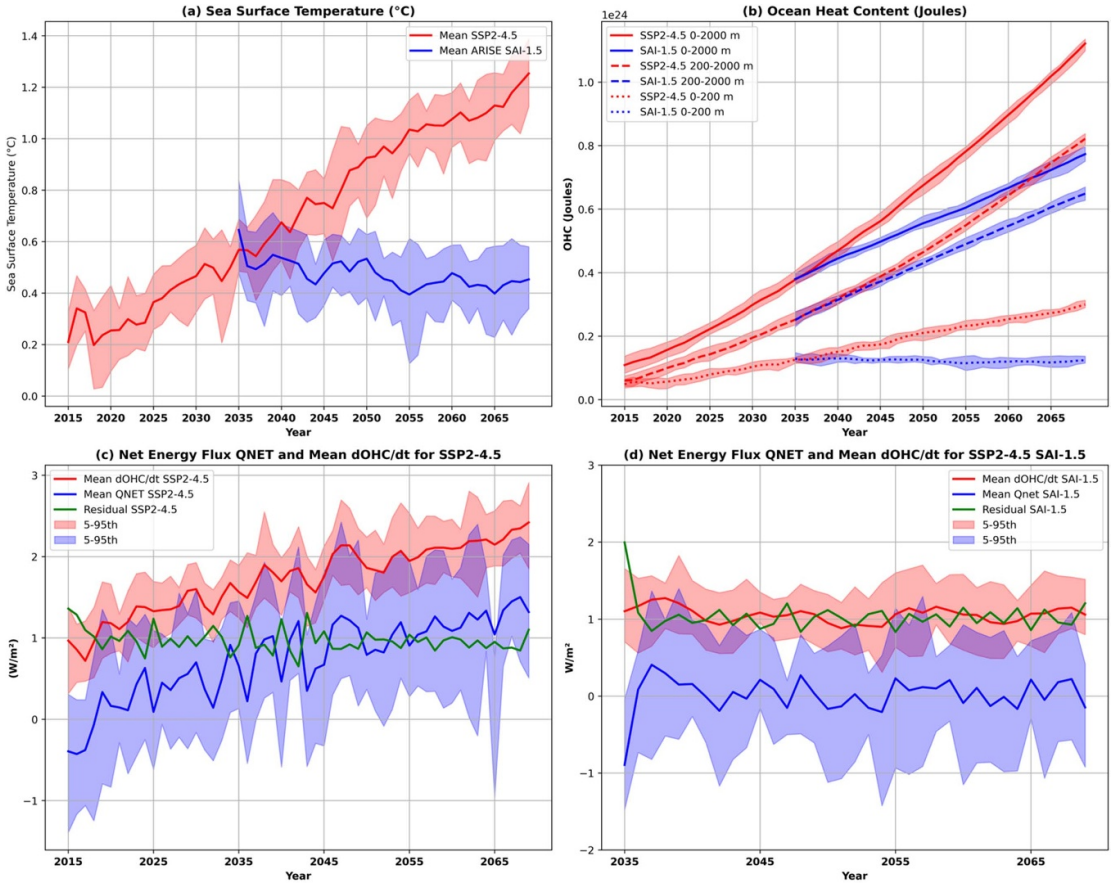

Figure 8. Time series of global (a) sea surface temperature changes, (b) ocean heat content changes, and (c) net surface energy flux (Q_{NET}) tendency of OHC changes, and the residual for SSP2-4.5 scenario (2015–2069) and (d) $Q_{NET,}$ tendency of OHC and dOHC/dt and the residual for SAI-1.5 (2035–2069). The shaded regions illustrate the 5th to 95th percentiles, highlighting the variability of the 10 members used for each scenario.

Table 2. Projected trends in OHC (10^{22} J yr^{-1}) estimated over different layers for SAI-1.5 and SSP2-4.5 scenarios, relative to 1995–2014.

Scenario	OHC (0–200 m)	OHC (200–2000 m)	OHC (0–2000 m)
SAI-1.5	−0.03	1.16	1.13
SSP2-4.5	0.50	1.68	2.19

shows a long-term trend, yet the residual remains nearly constant, similar in magnitude to that in the SSP2-4.5 case (figure 8(d)). This consistent residual suggests that the systematic nearly constant warming under both SSP2-4.5 and SAI-1.5 scenarios originates from the same underlying process. Under the SAI-1.5 scenario, this process occurs primarily below 200 m.

Figure 9 shows the evolution of global mean wind stress energy transfer changes to the ocean surface under SSP2-4.5 and SAI-1.5 scenarios, relative to the historical reference period (1995–2014). These values have been estimated by removing the historical mean values of wind energy transfer (from the reference period) from those of the SAI-1.5 and SSP2-4.5 scenarios. The ensemble mean trajectories reveal a clear divergence: SSP2-4.5 exhibits consistently higher and more variable wind stress energy transfer, while SAI-1.5 remains near zero throughout the period. The shaded bands represent the 5th–95th percentile range across ensemble members, highlighting the internal variability within each scenario. The muted wind stress forcing under SAI-1.5 reflects the impact of SAI on atmospheric circulation and surface momentum fluxes. This reduction in mechanical energy input may help explain the slower increase in surface-layer OHC observed under SAI-1.5, despite similar net surface heat flux (Q_{NET}) compared to SSP2-4.5. Wind stress energy transfer, as shown here, provides a complementary diagnostic to Q_{NET}, capturing the dynamical energy available for vertical mixing and heat redistribution. The figure highlights the importance of mechanical forcing in shaping near-surface ocean energetics.

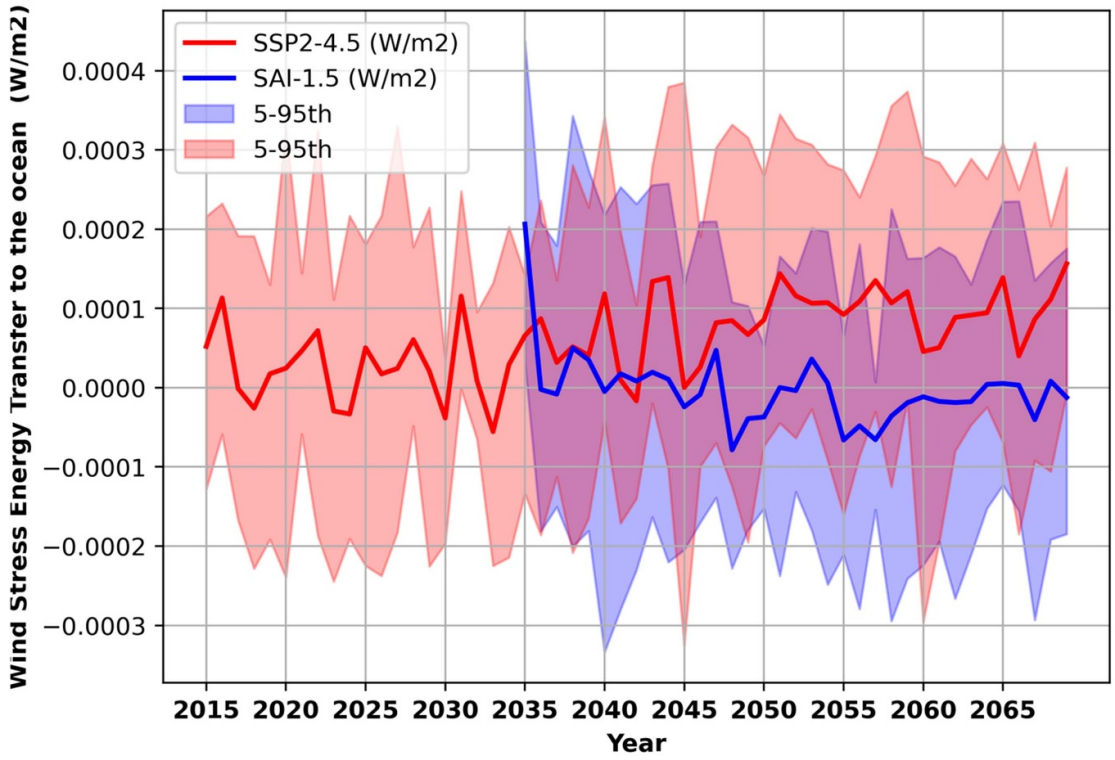

Figure 9. Projected wind stress energy transfer changes relative to the reference period from 1995 to 2014 for the ocean surface ($W \cdot m^{-2}$) under SSP2-4.5 and SAI-1.5 scenarios from 2015 to 2065. Solid lines represent the ensemble mean for each scenario (red: SSP2-4.5; blue: SAI-1.5), while shaded areas indicate the 5th–95th percentile range across ensemble members.

3.6. Global coastal sea level changes

Figure 10 illustrates projected changes in DSL and TSL along global coastlines under SSP2-4.5 and SAI-1.5 for the period 2050–2069 relative to the baseline of 2020–2039 (SSP2-4.5 scenario). In this study, the term, 'coastal region' refers to sea level values extracted at grid points adjacent to land boundaries, as defined by a coastline shapefile. This usage is informal and does not correspond to a predefined CESM coastal mask. The figure highlights regional variations in projected sea level change and the implications for coastal communities. Figure 10(a) shows DSL changes for SSP2-4.5 relative to baseline, revealing substantial increases in sea level, particularly along the eastern coast of North America and the western coast of Europe. These areas are facing heightened risks of flooding and erosion, threatening infrastructure and ecosystems. Conversely, some regions in the southern hemisphere, such as parts of South America and Australia, demonstrate relatively stable DSL values or projected decreases. Figure 10(b) illustrates the difference between DSL changes under SAI-1.5 and under SSP-2.45 for the period 2050–2069. While some regions, especially in the Arctic and Southeast Asia, project reduced rates of DSL increase, others, including the Caribbean and Gulf of Mexico, project continued rapid increases in DSL and associated risks. Figure 10(c) presents the change of TSL for the SSP2-4.5 scenario relative to the baseline. Regions like the Caribbean and Southeast Asia are particularly vulnerable, as increasing sea level is projected. Figure 10(d) shows changes in TSL under the SAI-1.5 scenario compared to SSP2-4.5 at the end of the simulation (2050–2069), most coastlines project a lower rate of TSL under SAI-1.5. Figures 9(e) and (f) combine DSL and TSL data for both scenarios. Figure 10(e) projects alarming sea level increases for the SSP2-4.5 scenario, relative to the baseline, along the coasts of South Asia and the eastern United States. In contrast, figure 10(f) shows the difference in projected total sea level change under SAI-1.5 relative to SSP-2.45. The results suggest that SAI-1.5 could mitigate the rate of SLR in the Arctic and parts of Europe, although all coastlines will continue to experience SLR, and some coastlines are projected to experience similar or increased rates as those projected under SSP2-4.5.

4. Discussion and summary

This study highlights the significant potential of SAI as a climate intervention strategy to mitigate the rate of SLR, and increases in OHC and thermal expansion compared to SSP2-4.5. This study differs from that of Yue *et al* [3] by calculating regional thermosteric sea level components at each grid cell rather

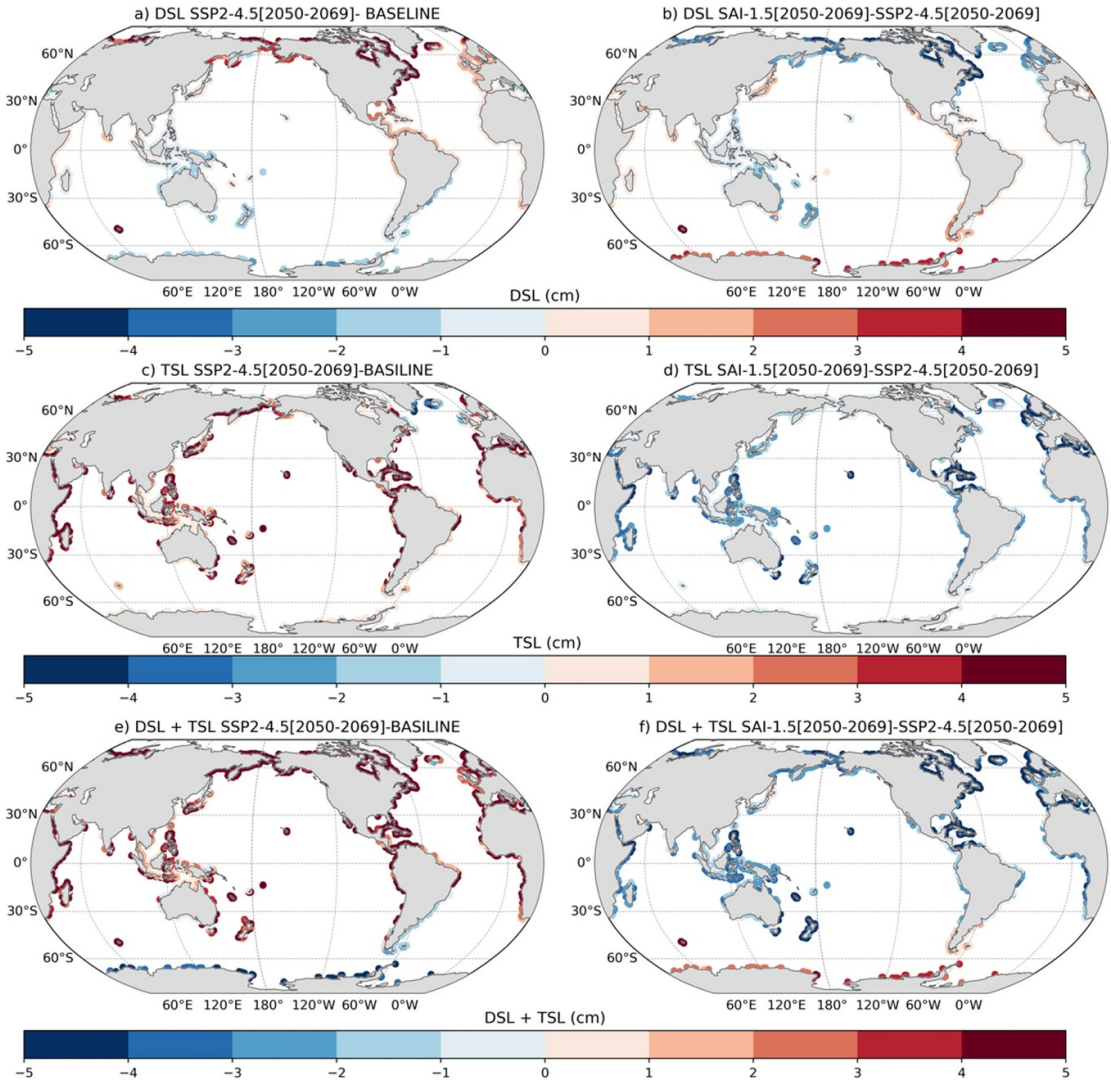

Figure 10. Projected dynamic and thermosteric sea level changes along global coastlines under two climate scenarios in 2050–2069. (a) Dynamic sea level (DSL, cm) for SSP2-4.5 relative to the baseline (2020–2039). (b) Difference in DSL changes for SAI-1.5 relative to SSP2-4.5 (2050–2069). (c) Thermosteric sea level changes (TSL, cm) for SSP2-4.5 relative to the baseline (2020–2039: SSP2-4.5). (d) Difference in projected TSL (cm) changes for SAI-1.5 relative SSP2-4.5 (2050–2069). (e) Combined dynamic and thermosteric sea level (DSL + TSL, cm) for SSP2-4.5 relative to the baseline (2020–2039). (f) Difference in Combined DSL and TSL (cm) changes for SAI-1.5 relative SSP2-4.5 (2050–2069).

than as a global thermosteric estimate. The research indicates that SAI can effectively stabilize global SST and OHC in the upper layers of the ocean, and reduce the rates of SLR but will not stop sea levels increasing. However, it also reveals complex dynamics in deeper ocean layers, where ongoing warming continues to occur, showing that SAI's effects are not uniform across all ocean depths.

One of the critical insights from the study is the importance of understanding regional variations in climate responses. The impacts of SAI differ across ocean basins and depths, and the regional contributions of thermosteric and DSL s highlight the necessity for comprehensive climate modeling that incorporates both thermosteric and halosteric effects. SAI can mitigate thermal expansion in vulnerable extratropical regions, demonstrating its potential utility in climate adaptation strategies. However, OHC continues to rise particularly between depths of 200–2000 m, highlighting the ongoing subsurface heat accumulation that contributes to long-term SLR. The study emphasizes that SAI should not be viewed as a standalone solution for addressing climate change impacts. SAI primarily focuses on reflecting sunlight to reduce surface temperatures but does not address other impacts of high atmospheric CO_2, such as ocean acidification and changes in marine ecosystems [30]. This study also reveals significant variations in SLR across global coastlines, with SAI-1.5 projecting a reduction in the rate of SLR along most coastlines, while SSP2-4.5 suggests more aggressive and widespread rises, especially along densely populated coastal areas. While SAI may alleviate some climate change impacts, substantial risks remain for some vulnerable coastlines mainly in the Southern Ocean.

The divergent wind stress energy transfer changes relative to the reference period from 1995 to 2014 under SSP2-4.5 and SAI-1.5 (figure 9) underscore the role of mechanical forcing in modulating ocean heat uptake beyond net surface heat flux (Q_{NET}) alone. While both scenarios exhibit comparable Q_{NET} trends, the markedly reduced wind stress energy transfer changes under SAI-1.5 suggests diminished mechanical energy input to the ocean surface, potentially limiting vertical mixing and delaying surface-layer warming. This aligns with findings by Kravitz *et al* [31], who noted persistent ocean heating under geoengineering despite near-zero Q_{NET}.

The continued rise in sea level and elevated subsurface OHC (200–2000 m) under SAI-1.5 likely reflects a combination of thermal expansion at depth, lateral and vertical heat redistribution [32], residual mechanical forcing [31], cryospheric freshwater input, and suppressed deep ocean ventilation [1]. These mechanisms highlight the importance of dynamical processes in shaping long-term ocean responses. The muted surface signal under SAI-1.5 should not be interpreted as a lack of ocean warming, but rather as a redistribution of heat into deeper layers, sustained by oceanic inertia and altered circulation [33].

One important limitation to note is that while CESM2 includes an interactive ice sheet model for Greenland (CISM2), the ocean model (POP2) does not account for the gravitational, rotational, and deformational (GRD) effects that come with land ice loss. These effects often called the 'sea level fingerprint' cause sea level to drop near the melting ice sheet and rise more strongly in regions farther away. Since POP2 does not simulate this redistribution dynamically, the patterns of DSL shown here reflect changes due to ocean circulation and density, but not the GRD signal.

This is particularly salient when interpreting regional sea level changes. For example, in areas far from Greenland, GRD effects can dominate the sea level response, and their absence in the coupled simulation means those patterns may be incomplete. While GRD adjustments can be estimated using offline tools, they are not part of the ocean model's internal physics. This remains a limitation in our interpretation and points to a clear direction for future model improvements that could better capture the spatial complexity of sea level change.

The vertical and regional patterns we find under SAI-1.5 show a broader signal emerging from recent ocean heat uptake studies. Li *et al* [34] showed that almost 90% of the heat gained by the global ocean since 2005 has been stored in mode and intermediate waters, with clear contrasts between basins and hemispheres. This perspective reinforces our result that even when SAI slows surface and upper-ocean warming, a significant share of excess energy still penetrates to depths of 200–2000 m. In practice, this means that the 'cooling' seen at the surface is more a reshuffling of heat into subsurface layers than an end to ocean warming. That redistribution has long-term consequences from thermal expansion driving continued sea-level rise to shifts in the circulation patterns that mode waters help sustain.

Data availability statement

The code to reproduce the figures will be available upon reasonable request. All 10 members of CESM2(WACCM6) SSP2-4.5 simulations and ARISE-SAI-1.5 simulations are freely available from the NSF NCAR Research Data Archive at https://doi.org/10.26024/0cs0-ev98 and https://doi.org/10.5065/9kcn-9y79. EN4 Ocean Salinity and Temperature data are downloaded from www.metoffice.gov.uk/hadobs/en4/ and the Sea Surface Height from data used in http://marine.copernicus.eu/documents/QUID/CMEMS-GLO-QUID-001-030.pdf [Dataset]. This study has been conducted using E.U. Copernicus Marine Service Information: https://doi.org/10.48670/MOI-00024.

Thermosteric & dynamic sea level analysis available at https://doi.org/10.1088/2752-5295/ae15b6/data1.

Acknowledgment

We would like to express our sincere gratitude to the NSF National Center for Atmospheric Research (NSF NCAR) for providing access to the GLADE (GLobally Accessible Data Environment) machine. The computational resources and data storage capabilities offered by GLADE have been instrumental in the successful completion of this study. We also extend our thanks to the NSF NCAR staff for their continuous support and assistance. Alan Robock is supported by NSF grant AGS-2017113.

Conflict of interest

All authors declare that there is no conflict of interest.

Author contributions

F B and A H wrote the manuscript with contributions from all the co-authors. A H performed the calculation of different sea level parameters with the contribution of F B. F B and A H made the figures with suggestions from all co-authors. A R, D V and M T edited the text.

Code Availability Statement

The data analysis and figure-drawing computer codes are written in python and are available from the corresponding author upon reasonable request. The regional and global sea level variables have been computer using https://momlevel.readthedocs.io/en/v0.0.11/ [Software].

Financial support

This work was supported by the Degrees Modelling Fund (formerly DECIMALS), a partnership between the Degrees Initiative and The World Academy of Sciences (TWAS). Alan Robock was supported by NSF grant AGS-2017113. This material is based upon work supported by the NSF National Center for Atmospheric Research, which is a major facility sponsored by the U.S. National Science Foundation under Cooperative Agreement No. 1852977. Support for BK was provided in part by NOAA's Climate Program Office, Earth's Radiation Budget (ERB) (Grant NA22OAR4310479), and the Indiana University Environmental Resilience Institute. The Pacific Northwest National Laboratory is operated for the US Department of Energy by Battelle Memorial Institute under contract DE-AC05-76RL01830.

ORCID iDs

Frédéric Bonou 0000-0002-2121-6893
Aubains Hounsou-Gbo 0000-0003-4278-6534
A Nathanael Dossa 0000-0001-5847-2455
Zacharie Sohou 0000-0003-3314-3481
Alan Robock 0000-0002-6319-5656
Ben Kravitz 0000-0001-6318-1150
Daniele Visioni 0000-0002-7342-2189
Mari Tye 0000-0003-2491-1020

References

[1] Fox-Kemper B *et al* 2021 Ocean, cryosphere and sea level change *Climate Change 2021: The Physical Science Basis. Contribution of Working Group I to the Sixth Assessment Report of the Intergovernmental Panel on Climate Change* ed V Masson Delmotte *et al* (*Cambridge University Press*) pp 1211–362
[2] Oppenheimer M *et al* 2019 Sea level rise and implications for low lying islands, coasts and communities *IPCC Special Report on the Ocean and Cryosphere in a Changing Climate* ed H-O Pörtner *et al* (*Cambridge University Press*) pp 321–445
[3] Yue C, Jevrejeva S, Qu Y, Zhao L and Moore J C 2023 Thermosteric and dynamic sea level under solar geoengineering *npj Clim. Atmos. Sci.* **6** 1–8
[4] Nicholls R J and Cazenave A 2010 Sea-level rise and its impact on coastal zones *Science* **328** 1517–20
[5] Irvine P J, Kravitz B, Lawrence M G and Muri H 2016 An overview of the Earth system science of solar geoengineering *WIREs Clim. Change* **7** 815–33
[6] Zahn M and Allan R P 2013 Climate warming–related strengthening of the tropical hydrological cycle *Am. Meteorol. J.* **36** 562–74
[7] Visioni D *et al* 2021 Identifying the sources of uncertainty in climate model simulations of solar radiation modification with the G6sulfur and G6solar geoengineering model intercomparison project (GeoMIP) simulations *Atmos. Chem. Phys.* **21** 10039–63
[8] Applegate P J and Keller K 2015 How effective is albedo modification (solar radiation management geoengineering) in preventing sea-level rise from the Greenland Ice Sheet? *Environ. Res. Lett.* **10** 084018
[9] Irvine P J, Sriver R L and Keller K 2012 Tension between reducing sea-level rise and global warming through solar-radiation management *Nat. Clim. Change* **2** 97–100
[10] Levin K, Waskow D and Gerholdt R 2021 *5 Big Findings from the IPCC's 2021 Climate Report* (World Resources Institute (WRI)) (available at: www.wri.org/insights/ipcc-climate-report)
[11] Danabasoglu G *et al* 2020 Large. The community earth system model version 2 (CESM2) *J. Adv. Model. Earth Syst.* **12** 1–35
[12] Riahi K *et al* 2017 The Shared Socioeconomic Pathways and their energy, land use, and greenhouse gas emissions implications: an overview *Glob. Environ. Change-Hum. Policy Dimens.* **42** 153–68
[13] Richter J H, Visioni D, MacMartin D G, Bailey D A, Rosenbloom N, Dobbins B, Lee W R, Tye M and Lamarque J-F 2022 Assessing responses and impacts of solar climate intervention on the earth system with stratospheric aerosol injection (ARISE-SAI): protocol and initial results from the first simulations *Geosci. Model Dev.* **15** 8221–43
[14] Gettelman A *et al* 2019 The whole atmosphere community climate model version 6 (WACCM6) *J. Geophys. Res. Atmos.* **124** 12380–4403

[15] Liu X, Ma P-L, Wang H, Tilmes S, Singh B, Easter R C, Ghan S J and Rasch P J 2016 Description and evaluation of a new four-mode version of the modal aerosol module (MAM4) within version 5.3 of the community atmosphere model *Geosci. Model Dev.* **9** 505–22
[16] MacMartin D G, Visioni D, Kravitz B, Richter J H, Felgenhauer T, Lee W R, Morrow D R, Parson E A and Sugiyama M 2022 Scenarios for modeling solar radiation modification *Proc. Natl Acad. Sci. USA* **119** e2202230119
[17] Global Ocean Ensemble Physics Reanalysis European Union-Copernicus Marine Service Information (CMEMS) Marine Data Store (MDS) *Global Ocean Gridded L4 Sea Surface Heights And Derived Variables Reprocessed Copernicus Climate Service GLO_PHY_CLIMATE_L4_MY_008_057* (https://doi.org/10.48670/moi-00145) (Acessed 12 June 2024)
[18] Cheng L, Zhu J, Cowley R, Boyer T and Wijffels S 2014 Time, probe type, and temperature variable bias corrections to historical expendable bathythermograph observations *J. Atmos. Ocean. Technol.* **31** 1793–825
[19] Levitus S, Antonov J I, Boyer T P, Locarnini R A, Garcia H E and Mishonov A V 2009 Global ocean heat content 1955–2008 in light of recently revealed instrumentation problems *Geophys. Res. Lett.* **36** 1–5
[20] Good S A, Martin M J and Rayner N A 2013 EN4: quality controlled ocean temperature and salinity profiles and monthly objective analyses with uncertainty estimates *J. Geophys. Res. Oceans* **118** 6704–16
[21] Gouretski V and Reseghetti F 2010 On depth and temperature biases in bathythermograph data: development of a new correction scheme based on analysis of a global ocean database *Deep Sea Res. I* **57** 812–33
[22] Griffies S M and Greatbatch R J 2012 Physical processes that impact the evolution of global mean sea level in ocean climate models *Ocean Model.* **51** 37–72
[23] Xu G, Chang P, Small J, Danabasoglu G, Yeager S, Ramachandran S and Zhang Q 2023 Enhanced upper ocean warming projected by the eddy-resolving community earth system model *Geophys. Res. Lett.* **50** 812–33
[24] Tim H J, Gregory J M, Palmer M D, Ringer M A, Katsman C A and Slangen A B A 2021 Projecting global mean sea-level change using CMIP6 models *Geophys. Res. Lett.* **48** 1–11
[25] Griffies S M *et al* 2014 An assessment of global and regional sea level for years 1993–2007 in a suite of interannual CORE-II simulations *Ocean Model.* **78** 35–89
[26] Huguenin M F, Holmes R M and England M H 2022 Drivers and distribution of global ocean heat uptake over the last half century *Nat. Commun.* **13** 1–11
[27] Hussain M M and Mahmud I 2023 pyMannKendall : a python package for non parametric Mann Kendall family of trend tests *J. Open Source Softw.* **4** 1556
[28] Oldenburg D, Kwon Y O, Frankignoul C, Danabasoglu G, Yeager S and Kim W M 2024 The respective roles of ocean heat transport and surface heat fluxes in driving Arctic Ocean warming and sea ice decline *J. Clim.* **37** 1125–46
[29] Flexas M M, Thompson A F, Torres H S, Klein P, Farrar J T, Zhang H and Menemenlis D 2019 Global estimates of the energy transfer from the wind to the ocean, with emphasis on near-inertial oscillations *J. Geophys. Res. Oceans* **124** 5723–46
[30] Zarnetske P L *et al* 2021 Potential ecological impacts of climate intervention by reflecting sunlight to cool Earth *Proc. Natl Acad. Sci.* **118** 1–11
[31] Kravitz B *et al* 2018 The climate effects of increasing ocean albedo: an idealized representation of solar geoengineering *Atmos. Chem. Phys.* **18** 13097–113
[32] Meyssignac B *et al* 2019 Measuring global ocean heat content to estimate the Earth energy imbalance *Front. Mar. Sci.* **6** 432
[33] Liu W, Lu J, Xie S-P and Fedorov A 2018 Southern Ocean heat uptake, redistribution, and storage in a warming climate: the role of meridional overturning circulation *J. Clim.* **31** 4727–43
[34] Li Z, England M H and Groeskamp S 2023 Recent acceleration in global ocean heat accumulation by mode and intermediate waters *Nat. Commun.* **14** 6888